The DOI for this manuscript is doi: 10.1175/JCLI-D-18-0071.1

Graffino, G., R. Farneti, F. Kucharski, and F. Molteni, 2018: The effect of wind stress anomalies and location in driving Pacific Subtropical cells and tropical climate. J. Climate. doi:10.1175/JCLI-D-18-0071.1, in press.

Draft of September 17, 2018

The effect of wind stress anomalies and location in driving Pacific Subtropical cells and tropical climate

Giorgio Graffino*

ESFM Doctorate School, Università degli Studi di Trieste, Trieste, Italy, and Earth System Physics Section, International Centre for Theoretical Physics, Trieste, Italy

Riccardo Farneti

Earth System Physics Section, International Centre for Theoretical Physics, Trieste, Italy

Fred Kucharski

Earth System Physics Section, International Centre for Theoretical Physics, Trieste, Italy, and Center of Excellence for Climate Change Research/Department of Meteorology, King Abdulaziz University, Jeddah, Saudi Arabia

Franco Molteni

European Centre for Medium-Range Weather Forecasts, Reading, United Kingdom

Corresponding author address: Giorgio Graffino, Earth System Physics Section, International Centre for Theoretical Physics, Strada Costiera 11, Trieste, Italy

E-mail: ggraffin@ictp.it

ABSTRACT

The importance of subtropical and extratropical zonal wind stress anomalies on Pacific Subtropical Cells (STCs) strength is assessed through several idealized and realistic numerical experiments with a global ocean model. Different zonal wind stress anomalies are employed, and their intensity is strengthened or weakened with respect to the climatological value throughout a suite of simulations. Subtropical strengthened (weakened) zonal wind stress anomalies result in increased (decreased) STCs meridional mass and energy transport. Upwelling of subsurface water into the tropics is intensified (reduced), a distinct cold (warm) anomaly appears in the equatorial thermocline and up to the surface, resulting in significant tropical sea surface temperature (SST) anomalies. The use of realistic wind stress anomalies also suggests a potential impact of mid-latitude atmospheric modes of variability on tropical climate through STC dynamics. The remotely-driven response is compared with a set of simulations where an equatorial zonal wind stress anomaly is imposed. A dynamically distinct response is achieved, whereby the equatorial thermocline adjusts to the wind stress anomaly resulting in significant equatorial SST anomalies as in the remotely-forced simulations, but with no role for STCs. Significant anomalies in Indonesian Throughflow transport are generated only when equatorial wind stress anomalies are applied, leading to remarkable heat content anomalies in the Indian Ocean. Equatorial wind stress anomalies do not involve modifications of STCs transport, but could set up the appropriate initial conditions for a tropical-extratropical teleconnection involving Hadley cells, exciting a STC anomalous transport which ultimately feeds back on the Tropics.

1. Introduction

Among all the interaction mechanisms relating the equatorial ocean to the extratropical and sub-tropical regions, the SubTropical Cells (STCs) are of paramount importance.

Their existence in the Pacific Ocean was theoretized by several works during the 1990s (McCreary and Lu 1994; Liu 1994; Lu et al. 1998), and was supported by observational (McPhaden and Zhang 2002, 2004; Zhang and McPhaden 2006) and modelling studies (Klinger et al. 2002; Nonaka et al. 2002; Solomon et al. 2003). STCs are meridional overturning circulations involving the subtropical-tropical region. They are shallow, extending from the surface to about 500 m depth. In the time-mean, a pair of STCs develop on each side of the Equator, consisting of a subtropical subduction branch, an equatorward advection in the subsurface layers, a sloped uprising in the equatorial thermocline, and finally a poleward return flow at the surface (Schott et al. 2004). Some important structural differences arise between the time-mean and the seasonal circulations (Nakano et al. 1999; Jayne and Marotzke 2001).

The upwelling component of the STC circulation involves the Equatorial Undercurrent (EUC), which feeds the thermocline at the Equator. The temperature of EUC water is in the range of 15°-25°C, meaning that the main source region must be located between 20° and 40° (Wyrtki and Kilonsky 1984), even though local recirculation of tropical waters can contribute as well.

The pathway followed by subducted water parcels is different between the two hemispheres. In the Northern Hemisphere the equatorward advection is limited, due to the presence of a high potential vorticity (PV) ridge close to 9°N (Lu and McCreary 1995; McPhaden and Zhang 2002). The PV ridge causes the water to take a longer route to reach the Equator (Johnson and McPhaden 1999; Johnson 2001). Therefore, water flowing from the northern Pacific Ocean to the Equator is made of two components: the western boundary part, and the interior part. The splitting of the

equatorward flow in two components occurs in the Southern Hemisphere as well, but to a lesser extent. Decadal variations of western boundary and interior components are almost out-of-phase, but STC variations are mainly locked to the interior component (Lee and Fukumori 2003).

Other overturning cells exist in the tropical region, such as the Tropical Cells (TCs). TCs are driven by the decrease of Ekman poleward transport occurring at about 5° off the Equator (Molinari et al. 2003). Despite their intensity, TCs are associated with a small meridional energy transport (Hazeleger et al. 2000), but force us to be cautious on the assessment of STC properties.

STCs exert a large impact on the tropical ocean, since they can act as "ocean tunnels" (Liu and Alexander 2007), for example by altering the energy transport in the Subtropics (Klinger and Marotzke 2000) and driving thermal anomalies at the Equator (Farneti et al. 2014a). On the other hand, the effect of local equatorial wind stress forcing is also significant in driving equatorial anomalies, as Nonaka et al. (2002) showed for decadal and interannual SST variability by forcing an ocean model with observed wind stress forcing. However, since Nonaka et al. (2002) focused on the analysis of the equatorial SST anomalies, the relative importance of local versus remote wind stress forcing must be better quantified and the STCs dynamics investigated. Furthermore, STCs have been used to explain some decadal-scale variability in the Pacific Ocean (Capotondi et al. 2005), due to their influence on ENSO (Kleeman et al. 1999) and their relation with the Pacific Decadal Oscillation (PDO) (Farneti et al. 2014b; Hong et al. 2014). The shallow-water modelling study by McGregor et al. (2007) showed that approximately 80% of the equatorial thermocline variability driven from the off-equatorial region is transferred to the Equator through Rossby wave reflection at the western boundary, with the remaining 20% ascribed to meridional mass transport. However, the transition between negative to positive PDO in the 1970s seems related to a concomitant slowdown of the STCs (McPhaden and Zhang 2002), with a "rebound" in the 1990s after another reversal of the PDO phase (McPhaden and Zhang 2004). In particular,

the first regime shift seems to be responsible for an increase of 0.8°C in the tropical Pacific Ocean sea surface temperature (SST) from the 1970s to the early 1990s (Zhang et al. 1997).

Schott et al. (2007) assimilation model reduced STC variations to only 40% of the value found by McPhaden and Zhang (2002), which however are reproduced again using a different forcing product (Schott et al. 2008). STC decadal variability can also be reproduced using both ocean-only (Farneti et al. 2014a) and coupled models (Solomon and Zhang 2006; Zhang and McPhaden 2006).

Gu and Philander (1997) exploited STC dynamics to explain the propagation of thermal anomalies originated in the North Pacific (Deser et al. 1996) to the equatorial regions (the so-called $\overline{v}T'$ mechanism), although the observational study of Schneider et al. (1999) suggested that temperature signals would decay quickly away from their source region. Another interpretation of the STCs observed influence on tropical dynamics was given by Kleeman et al. (1999), who suggested that subtropical wind stress forcing was able to alter the equatorial temperature structure, by changing the strength of those shallow meridional circulation structures (the so-called $v'\overline{T}$ mechanism).

Recently, England et al. (2014) linked STC dynamics to the recent global warming slow-down, which happened concurrently with a negative phase of the Interdecadal Pacific Oscillation (IPO) (Power et al. 1999; Meehl et al. 2013), corresponding to a cool tropical Pacific Ocean and an enhanced trade winds forcing. By linearly increasing the zonal wind stress forcing on the Pacific Ocean between 45°N and 45°S, England et al. (2014) accounted for a substantial heat content increase in the Indo-Pacific Ocean below 125 m and a decrease above 125 m.

The two-layer model of McCreary and Lu (1994) shows that the strength of the STCs is related to the zonal wind stress at a cutoff latitude for subtropical subduction, set to 18°. Thus, the amount of water reaching the Equator is mainly remotely determined at subtropical latitudes, which is consis-

tent with Pedlosky (1987) model, and not locally driven by the equatorial upwelling as suggested by Bryan (1991). The role of subtropical and extratropical zonal wind stress on the STCs forcing is explored in more detail by Liu and Philander (1995) with an idealized rectangular basin ocean set of simulations, showing that the subtropical wind stress forcing is able to significantly change the tropical temperature field, but with a limited influence on the EUC transport. Afterwards, Klinger et al. (2002), using the same 3-1/2 layer model of Lu et al. (1998) on a simplified representation of the Pacific Ocean, performed experiments using both steady and oscillatory forcing in different sectors of the Pacific Ocean, finding an almost linear relationship between the strength of the subtropical wind stress and the STC transport in steady-state conditions. Their oscillating experiments also show that an "optimal" forcing time period must exist, giving the biggest equatorial response. Klinger et al. (2002) finally underline the role of high-latitude anomalies on the ocean state at the Equator.

Among the observed mid-latitude atmospheric modes of variability, the Cold Ocean - Warm Land (COWL) pattern (Wallace et al. 1995, 1996) is particularly prominent over the Pacific Ocean. It is a circulation regime occurring in the Northern Hemisphere anomalously-warm cold season months, manifesting as a tendency for positive 1000 – 500 hPa thickness over the continents and negative values over the oceans, with respect to the hemispheric average. As such, the COWL corresponds to warmer-than-normal continents and colder-than-normal oceans. According to coupled model simulations, the primary cause of such pattern is the different thermal inertia of ocean and land, whereas the role of dynamical air-sea interactions seems less important (Broccoli et al. 1998). Molteni et al. (2011) provided a dynamical interpretation of the COWL regime in terms of planetary waves, being the positive phase of a hemispheric-wide "thermally balanced wave mode".

Molteni et al. (2017) showed that the global warming slow-down was accompanied by strong COWL-related wind stress anomalies in the northern subtropics and extratropics. One of the

questions raised in Molteni et al. (2017) was if such wind stress anomalies could be relevant in contributing to turn the global warming slow-down into a period of accelerated warming by inducing positive decadal SST anomalies in the equatorial Pacific region, as suggested by Farneti et al. (2014b).

Using idealized and realistic wind stress patterns and intensities, at different latitudes ranging from equatorial to extratropical, we test here some of the previously proposed hypotheses. In particular, we aim to quantify the relative importance of equatorial, subtropical and extratropical wind stress on driving STC mass and energy transport anomalies, which is also strictly related to the possibility of driving temperature and circulation anomalies at the Equator.

The paper is organized as follows. In Section 2 the setup of our numerical experiments is detailed, results are described in Section 3. Discussions and conclusions are given in Section 4.

2. Model and Experiments

We employed the NOAA/GFDL Modular Ocean Model version 5 (MOM5; Griffies 2012), a global-ocean, volume-conserving, primitive equations model. The horizontal resolution is $1^\circ \times 1^\circ$, with a finer discretization from 30°N to 30°S in the meridional direction. The model has 50 vertical levels in depth coordinates and 80 levels in potential density coordinates. Subgrid mesoscale processes are parameterized using the Gent-McWilliams skew-flux closure scheme (Gent and Mcwilliams 1990; Gent et al. 1995; Griffies 1998), and submesoscale eddy fluxes are parameterized following Fox-Kemper et al. (2008, 2011).

Boundary conditions are imposed at the sea surface, where the climatological CORE Normal Year Forcing (NYF) atmospheric state is used (Griffies et al. 2009). Surface fluxes of heat, freshwater and momentum are determined using the CORE NYF atmospheric data sets, the model's prognostic SST and surface currents, and the bulk formulae described in Large and Yeager (2009).

There is no restoring term applied to SSTs. In contrast, surface salinity restoring is used to prevent unbounded local salinity trends, with a relaxation timescale of 60 days.

We performed a long control run in order to obtain a statistically stable mean state. After about 4000 years the model had adjusted in its deep layers, and standard metrics showed minimal drift. Stability was evaluated in terms of mass transport of the Antarctic Circumpolar Current at the Drake Passage, and the global Meridional Overturning Circulation at some key locations. No significant drift was observed, although some low-frequency oscillations occur in some time series.

Starting from the last 200 years of the control run, we performed several perturbation experiments using time-constant wind stress anomalies (Table 1). Each zonal wind stress anomaly used in the simulation is obtained as a fraction of the climatological value, and then added to or subtracted from the NYF field. Figure 1 shows the zonal average of the zonal wind stress anomalies. Zonal wind stress anomalies, superimposed on the NYF forcing, are chosen according to their geographical pattern and location, or by choosing a proper wind stress threshold that would maintain continuity with the climatological contours (Figure 2a). For each case, ten experiments are performed (Table 1) in order to assess the possibility of a linear relationship between the forcing applied and the STCs response. Anomalous forcing experiments are 20 years long, and we show results averaged over the last 5 years.

Building on the results from these idealized experiments, we also performed a complementary smaller set of simulations, designed to assess the influence of COWL-related wind stress forcing on the STCs. Two different zonal wind stress anomaly pattern are employed, both derived from ensemble members of the ECMWF seasonal forecast system-4 (Molteni et al. 2017). One wind-stress anomaly pattern (*COWL*) was generated to match as close as possible the observed COWL-type wind-stress difference between the two periods 2009/2013 and 1996/2000 (Fig. 2g), while the other (*NOCOWL*; Fig. 2h) was designed to have no projection on the COWL pattern (see

Molteni et al. (2017) for details). It should be noted that both patterns have very similar equatorial wind stress anomalies, while they differ substantially in subtropical and extratropical regions. Furthermore, being derived from ensemble members of the ECMWF seasonal forecast, they are also both dynamically consistent wind stress anomaly patterns. Anomalies are added or subtracted from the NYF field. Thus, by analyzing the difference in the response between the experiment *COWL* and *NOCOWL*, we were able to investigate the impact of observed decadal off-equatorial wind-stress anomalies on the STCs as well as on equatorial thermocline and temperature.

Our main purpose is to assess the effect of subtropical and extratropical wind stress on STCs dynamics, and how their transport modifications propagate and influence the equatorial state. We carried out similar analyses on a set of equatorial experiments, in order to have a direct comparison between locally- and remotely-forced perturbation anomalies.

a. Volume and energy flux diagnostics

We compute the total meridional mass transport (in Sverdrups; 1 Sv = 10^6 m^3 s^{-1}) as

$$\Psi(y,z) = -\int_{\lambda_1}^{\lambda_2} \mathrm{d}x \int_{-h}^{\eta} \mathrm{d}z' \, (v + v^*), \tag{1}$$

where λ_1, λ_2 define the longitudinal extension of the basin, h is the ocean's depth, η is the sea surface, and the transport includes both resolved v and parameterized v^* meridional velocities. Given that we are interested in the volume and energy anomalies reaching the Equator, in most of our analysis we only consider the zonally and vertically integrated equatorward meridional transports in the uppermost 1000 m.

The meridional total energy transport (PW = 10^{15} W) is computed as an anomaly of the control run value, namely

$$E_{TOT}(y) = \rho_0 C_\mathrm{p} \int_{\lambda_1}^{\lambda_2} \mathrm{d}x \int_{-h}^{\eta} \mathrm{d}z \, (vT - v_c T_c), \tag{2}$$

where ρ_0=1035.0 kg m^{-3} is the reference density, C_p=3992.1 J kg^{-1} °C^{-1} is the heat capacity for seawater at constant pressure (Griffies 2012), v is now the total meridional velocity component and T is potential temperature for the perturbation experiment, whereas v_c and T_c relates to the control run.

The above diagnostic produces the full energy flux anomaly in the chosen latitudinal range. In order to isolate the contribution from the STCs, the energy transport calculation proposed by Klinger and Marotzke (2000) is also used, where only zonal wind stress and SST values are needed. As shown in Section 3e, wind-driven meridional mass transports and meridional SST gradients are exploited to compute the meridional energy flux ascribed to STCs only.

Ocean heat content (OHC) is also evaluated as an anomaly, that is

$$OHC = \rho_0 C_\mathrm{p} \int_{\lambda_1}^{\lambda_2} \mathrm{d}x \int_{\phi_1}^{\phi_2} \mathrm{d}y \int_{-h}^{\eta} \mathrm{d}z\,(T - T_c). \tag{3}$$

Finally, the Indonesian ThroughFlow (ITF) accounts for the exchange of water between Pacific and Indian basins. It is computed summing up the zonal transport crossing the passage between South Timor and Australia, and the meridional transport passing through Lombok and Ombai Straits.

3. Results

We designed our experiments to test the sensitivity of a time-constant zonal wind stress anomaly on the STCs, located at some specific latitudinal range. Thus, they are not meant to reproduce any observed variability, but rather to quantify and test the sensitivity of STCs to idealized and realistic forcing anomalies. Although the absolute value of the imposed surface anomalies lies between the observed variability at both Subtropics and Extratropics (not shown), their duration is not realistic and serves the purpose of testing different hypotheses.

a. Equatorial Anomalies

Ten experiments were performed imposing a zonal wind stress anomaly at the Equator (Figure 2b). Five experiments have strengthened wind stress anomalies added on the climatological forcing in that region, five have instead weakened anomalies. The pattern extends from 8°N to 8°S in latitude and from 170°E to 100°W in longitude, with values smoothed linearly to zero at the edges. The shape is similar to the region defined by England et al. (2014) as the IPO-related contribution to the strengthened trade winds circulation in the Pacific Ocean. The equatorial experiments assess the impact of zonal wind stress anomalies at the Equator on the STCs.

Figure 3 shows the time series of equatorward mass transport at 9°N and 9°S, at the boundaries of the anomaly. The meridional transport from each experiment is zonally-integrated on the whole Indo-Pacific basin, vertically-integrated in the first 1000 m, and finally subtracted from the control value. At 9°N, an increasing divergence of the equatorward mass transport from the control value is observed as the magnitude of the zonal wind stress anomaly increases. Instead, at 9°S the behavior is more chaotic, probably due to the contribution of the Indian Ocean in the computation. However, equatorial mass transport anomalies are less than a tenth of the control value.

The top panels in Figure 4 show the anomalous transports for some selected experiments. For convenience, we show only results for the strengthened anomalies. Even though the impact of the equatorial wind stress anomalies on the overturning circulation is significant, the signal is confined to 10°N-10°S and to a limited potential density range (1030-1032 kg/m^3), and thus does not involve the Subtropics. An equatorially-confined wind stress anomaly, however strong, is only able to force local overturning structures very close to the Equator, such as the Tropical Cells, but not the STCs.

Meridional energy transport anomalies are restricted to a small latitudinal extent across the Equator (not shown). Since TCs act over a weak temperature gradient their energy transport is limited, even in the case of strong wind stress forcing.

The zonal velocity structure driven by the equatorial anomalies is a dipole. In Fig. 4 (central panels), positive (negative) velocity anomalies in the lower (upper) pycnocline are obtained from the strengthened experiments; the pattern is reversed for the weakened experiments (not shown).

A thermal response at the Equator is clearly showed in Figure 4 (bottom panels), larger in the western Pacific Ocean and with anomalies up to 3°C. As we will show later, these signals are different from a typical STCs response (see central panels in Fig. 8), being related to a local adjustment of the thermocline to the wind stress forcing, rather than to a remote advection from the STCs. In fact, a stronger (weaker) zonal wind stress at the Equator pushes more (less) efficiently the surface water towards the west, and the equatorial thermocline tilt is enhanced (reduced). For strengthened wind stress anomalies, a steeper thermocline results in a warm anomaly in the west Pacific and a cold anomaly in the east Pacific.

At the surface, a typical La-Niña condition develops for strengthened anomalies (Figure 5), with a cold SST anomaly (up to 1°C) developing at end of the simulations along the Equator. Conversely, the weakened experiments build up an El-Niño SST pattern. This temperature response is quite remarkable, since the NYF atmospheric state at the surface is constantly damping any ocean thermal anomaly, constraining the simulated SST toward the climatological atmospheric state.

By changing the equatorial wind stress strength, we are also changing the mass transport across the Indonesian straits (Fig. 6). The anomaly of the Indonesian ThroughFlow (ITF) transport for the strongest experiments is up to 2 Sv, or about 15% with respect to the control transport of 11-12 Sv. Furthermore, the strength of the transport anomaly is similar to what has been estimated by previous studies (Meyers 1996; England and Huang 2005). It also explains the different behavior

between the STCs mass transport time series in the Northern Hemisphere (Fig. 3, left panel) and in the Southern Hemisphere (Fig. 3, right panel). In fact, as the mass transport integration (Eq. 1) is performed on the whole Indo-Pacific basin, the time series at 9°N is poorly influenced by the Indian Ocean contribution, whereas the altered ITF transport and the related changes in the Indian Ocean circulation strongly affects the computation at 9°S. As soon as the wind stress anomaly sets on, the ITF transport is modified with little delay. Then, it decays for some time before stabilization. The effect of the altered ITF transport on the Indian Ocean is displayed by a clear SST signal, as well as a modified ocean heat content in the upper Indian Ocean (not shown).

b. Subtropical Anomalies

The main STCs driving mechanism occurs through changes of the wind stress at the Subtropics (McCreary and Lu 1994). Therefore, we expect the STCs response to be the largest when a wind stress anomaly is located in those regions. We performed twenty experiments (ten in each hemisphere), employing both strengthened and weakened anomalies (Figure 2c, e).

As shown in Figure 7, the effect of the subtropical anomalies is large on the STCs mass transport, up to 10-12 Sv for the strongest experiments at 15° in each hemisphere; at its maximum, the anomalous transport is roughly one third of the control value for both hemispheres. The stabilization of the trends occur on a decadal time scale, and is faster for the Northern Hemisphere experiments.

Some examples of the structure of the STCs response are showed in Figure 8. Compared to the equatorial anomalies (Figure 4), here we can see a proper response of the STCs involving the whole overturning structure from the Equator to the subtropical region. Only the Northern Hemisphere experiments are showed, being the Southern Hemisphere response very similar.

A broad meridional ocean energy transport anomaly, straddling the whole subtropical and tropical regions, is obtained for both Northern and Southern Hemisphere experiments (not shown). The anomalous energy transport spans the whole subtropical region, with anomalies ranging from 0.03 PW (10% of the control value) for the 10% experiment to 0.3 PW (60% of the control value) for the 50% experiment. It should be noted that the computation includes the Indian Ocean transport, affecting the Southern Hemisphere estimate. A linear relationship between meridional energy transport and wind stress holds, mainly for small anomalies. For larger anomalies (40% and 50%) this relationship is lost. In fact, large wind stress anomalies are affecting not only the STCs, but significantly modify energy transports related to the wind-driven gyre.

By changing the STCs transport, subtropical wind stress anomalies are able to drive a considerable response at the Equator (Figure 8, central and bottom panels). Comparing our subtropical results with the equatorial ones (Figure 4), we can see how the two responses are significantly different. In the equatorial experiments, even though the thermal signal can be stronger locally, as in the west Pacific, we do not see any STC-related effect. Instead, cold anomalies arising in the equatorial thermocline from the strengthened subtropical wind stress anomalies can be traced to a remote response due to the STCs (Figure 8). Indeed, an accelerated STC is able to draw deeper (and colder) water to the Equator, by feeding the EUC (Fig. 8, central panels). Similarly, weakened subtropical wind stress anomalies drive warm anomalies at the Equator by slowing the EUC and reducing the local upwelling of relatively cold waters. In this respect, our results differ from the conclusions given by Liu and Philander (1995), whose EUC response is said to be very limited, which is not the case in our experiments (not shown).

Looking at the sea surface (Figure 9), a cold SST signature develops from the 20% strengthened experiment onwards. A warm response is instead obtained in the weakened experiments (not shown). Considering only the north-subtropical experiments, both strengthened and weakened

50% wind stress anomalies force a response up to 0.48°C in the Niño 3.4 region. South-subtropical experiments drive a slightly smaller thermal signal. These values are very close to the threshold (0.5°C, https://www.ncdc.noaa.gov/teleconnections/enso/indicators/sst.php) associated to a warm or cold ENSO phase. The equatorial SST adjustment time is faster for the northern subtropical experiments, being part of the wind stress anomaly very close to the Equator (not shown). Instead, the southern subtropical wind stress anomaly takes up to 10 years to force an equatorial response.

There is no significant anomaly in the ITF transport in any of the subtropical experiments (not shown). This result indicates that strengthening or weakening subtropical wind stress does not lead to any appreciable modification of the ITF mass transport.

c. Extratropical Anomalies

We showed how a subtropical zonal wind stress anomaly can influence STC dynamics. Our next purpose was to verify whether such influence could occur with an anomaly located further poleward. Indeed, many mid-latitude weather regimes are related with characteristic zonal wind stress patterns in the Pacific sector.

We performed two sets of experiments imposing idealized extratropical anomalies, extending up to 45° in each hemisphere, with a linear smoothing at the edges of the anomaly. As before, the intensity of the anomaly was a fraction of the climatological zonal wind stress (Table 1). In one set, the wind stress anomaly reached into the Subtropics, as far as 15°, whereas the second set started at 20°, and it is considered purely extratropical (Fig. 2d, f).

A remarkable STC response, able to force a stable thermal signal in the equatorial thermocline up to the surface within 12 years, is only found in the case where anomalies reached the edge of the subtropical gyre (not shown). On the contrary, any significant STC response is vanished, as well as the thermal equatorial signal, when using purely extratropical wind stress anomalies. Presumably,

all anomalous mass transport generated at 20° recirculated within the subtropical gyre, without reaching the equatorial region. This result confirms that STCs are mainly forced by wind stress at the cutoff latitude for subtropical subduction, around 15°-20°, the edge of the subtropical gyre.

d. COWL Anomalies

We then made a step further and considered the effect of realistic decadal wind stress anomalies on STCs. A wind stress anomaly associated with observed decadal COWL variability was selected because of its potential to contribute to global warming slow-downs or accelerations (Farneti et al. 2014b; Molteni et al. 2017).

Two zonal wind stress anomaly patterns are obtained from the ECMWF forecasting system-4. One reproduces the observed decadal off-equatorial COWL-related wind stress anomaly from the period 2009/2013 compared to 1996/2000 (referred to as *COWL*; see Fig. 2g). The second anomaly is obtained as a difference from the same periods, but from ensemble members not projecting on the COWL pattern (referred to as *NOCOWL*; see Fig. 2h). A series of experiments are performed by adding these anomalies to or subtracting them from the NYF field, without altering their intensity.

The time series at 15° N (Fig. 10) shows the response of the equatorward mass transport to the applied wind stress anomalies. The *COWL* pattern modified the mass transport by ≈2 Sv, stabilizing after about 5 years. The signal generated by the *NOCOWL* pattern stabilized earlier with a maximum value of 0.8 Sv.

The main difference between the two applied wind stress patterns lies outside the Equator. Our conclusions in Sec. 3a highlighted the role of equatorial wind stress as the main driver of anomalies in that region. Hence, the potential signal forced at the Subtropics is likely to be obscured by the

locally-generated response. Therefore, in the following we analyze the difference between both ensemble means, so highlighting any subtropically-generated signal.

As seen in Fig. 11 (top panels), the off-equatorial zonal wind stress related to the COWL regime is able to force a distinct STC response in the Northern Hemisphere. This anomalous mass transport alters the velocity structure in the equatorial thermocline (Fig. 11, central panels), driving a thermal signal through the same process we described in Sec. 3b, up to 0.4°C (Fig. 11, bottom panels). The response is nearly symmetrical for strengthened and weakened experiments.

At the surface, a warm (cold) SST signal is generated at the Equator in the Pacific Ocean for strengthened (weakened) COWL wind stress anomalies (Fig. 12). The equatorial response develops along the whole basin, with a maximum value of 0.1°C in the eastern Pacific. Also, the sign of the anomaly is consistent with the sign of the subtropical wind stress of the *COWL* anomaly (Fig. 2g). The response time of both *COWL* and *NOCOWL* experiments is very similar to what was obtained with our idealized equatorial wind stress anomalies (not shown), again highlighting the fundamental role of the local wind stress forcing on the equatorial ocean state.

e. Meridional energy transport by the STC

The meridional energy transport calculations presented so far included all dynamical processes, which in the Pacific mainly involves the STCs and the wind-driven gyre contributions. In order to isolate the STCs contribution we employed the method developed by Klinger and Marotzke (2000), which allows the computation of the STC-related meridional energy transport using Ekman dynamics. The expression for the STC meridional energy transport is

$$\mathrm{E_{STC}}(y) = C_\mathrm{p} \int_{\lambda_1}^{\lambda_2} \mathrm{d}x \int_{y_1}^{y} \mathrm{M_E} \frac{\partial \theta}{\partial y} \mathrm{d}y, \tag{4}$$

where $M_E = -\tau(y)/f(y)$ is the Ekman mass transport and θ the surface potential temperature. The energy transport is integrated zonally and for each model grid point between 10° and the latitude of zero wind stress (≈30°), although the contribution to STC mass transport in the real ocean can come from a more northern location (McCreary and Lu 1994; Liu et al. 1994). A full derivation of Eq. 4 is provided in the Appendix.

First, we computed the estimates for the STC meridional energy transport in our control run and for all basins (Fig. 13). Our model results compare well with the observational estimates given in Klinger and Marotzke (2000, c.f. Fig. 6). Because of their zonal extent, Pacific and Indian Ocean STCs stand out with the largest meridional fluxes.

In Fig. 14 we compute STCs meridional energy transport anomalies generated by the equatorial, northern subtropical and *COWL* wind stress anomalies. As expected, equatorial experiments produce very weak anomalies (Figure 14a, d), with some significant deviations from the control state only within the equatorial region. Subtropical (Fig. 14b, e) experiments are instead associated with large STC meridional energy transport anomalies, extending up to 20°. Meridional energy transport anomalies directly related to STCs account for ≈1/3 of the total transport anomaly. The relative role of STCs is larger for modest anomalies, whereas it becomes less important for the strongest cases. This is probably due to the intensification of the wind-driven subtropical gyre, transporting large amount of heat poleward. STC meridional energy transport anomalies obtained from *COWL* realistic wind stress patterns (Fig. 14c) extend up to 25°, and are comparable to the 20% anomaly subtropical experiments. *NOCOWL* induced anomalies are close to zero, confirming the significant role played by the subtropical sector of the COWL regime on STCs energy transport.

4. Discussions and conclusions

We studied the effect of different wind stress patterns, located in different areas of the Pacific Ocean, on the Pacific SubTropical Cells (STCs). Employing a global ocean model (MOM5; Griffies 2012), we applied idealized and realistic time-invariant zonal wind stress anomalies at the sea surface, strengthening or weakening the climatological forcing. We note that the observed interannual variability of the zonal wind stress in Pacific subtropical and extratropical regions can produce anomalies even larger than the one used in this study (not shown). Results from the different perturbation experiments were compared with respect to a climatologically-forced long control run. In England et al. (2014) a zonal wind stress anomaly was applied to the entire Pacific basin from 45°N to 45°S. We chose here to test the STC response by using selected forcing locations, in order to understand which region gives the strongest STC response.

In general, the equatorial response produced by trade winds anomalies is stronger than the one generated from outside the tropics. In fact, by changing the wind stress forcing on a very large area, the largest part of the off-equatorial signal could be hidden by the (relatively larger) locally-generated response. In fact, the structure of the meridional overturning circulation trend in England et al. (2014) is very similar, in terms of spatial extension, to what is obtained here with equatorial wind stress anomalies (Figure 4).

Our results can be summarized as follows.

- Equatorial wind stress anomalies located between 8°S and 8°N do not extend poleward enough in order to force the STCs. Zonal cross sections at the Equator showed large thermal anomalies (up to 3°C) in some cases, but they are related to an adjustment of the thermocline in response to the different local wind stress forcing. Appreciable changes in ITF transport

are also obtained (up to 2 Sv), leading to a remarkable temperature anomaly in the Indian Ocean (not shown).

- Among all experiments, subtropical wind stress anomalies have the strongest impact on STCs. Equatorward mass transport anomalies reach 12 Sv, roughly one third of the control value. The generated STCs motion develops mainly in the thermocline, with a striking thermal signal appearing at the Equator: up to 1°C at depth and 0.5°C at the surface. In terms of energy transport, anomalies reach close to half of the control value for the experiment with the strongest wind stress anomaly. However, if a diagnostic for STC-related meridional energy transport is used, then STCs energy flux is quantified to be $\approx$1/3 of the total transport anomaly. Finally, subtropical wind stress anomalies – and the associated STC dynamical changes – do not have an appreciable effect on ITF transport.

- Extratropical wind stress anomalies are found to exert a weak influence on both mass and energy STCs transport, as compared to subtropical experiments. In particular, most of the signal is forced within the 15°-20° region, as evidenced by a set of forcing anomalies located north to those latitudes which did not produce appreciable changes in STC dynamics. In the latter case, transport anomalies likely recirculate within the subtropical gyre.

- Finally, the observed COWL-related zonal wind stress patterns are able to force a signal from the northern STC reaching the Equator, with a thermal anomaly of 0.4°C in the thermocline and 0.1°C at the surface.

The overall behavior of the northern-hemisphere idealized experiments is summarized in Figure 15, where anomalies in equatorward mass transport, STC energy transport and equatorial SST are plotted against values of anomalous wind stress forcing.

Equatorial experiments are not able to drive a substantial response in terms of either mass or energy transport. In fact, however strong, equatorial wind stress anomalies are always related to a local dynamical adjustment, with a thermal signal due to the the adjustment of the thermocline to the changing wind stress at the surface. Thus, here only the shallower Tropical Cells are excited. Even though the equatorial wind stress anomalies do not involve modifications of STCs transports, they could in fact set up the appropriate initial conditions for a tropical-extratropical teleconnection, whereby the thermally-direct Hadley cell anomalies can produce subtropical wind stress and wind-stress curl changes leading to STC anomalous transports feeding back to the Equator resulting in opposite anomalies there, as hypothesized in Farneti et al. (2014b). The oceanic component of this oscillation was further tested and quantified here, however the complete cycle can only be reproduced within a coupled model, and not in our ocean-only setup which is also damping our surface anomalies due to the imposed atmospheric state.

SST anomalies in the Niño 3.4 region are larger for the equatorial experiments, stressing the importance of local wind stress forcing on the equatorial ocean state. Despite the climatological atmospheric surface temperature applied to the model, remotely-induced thermal anomalies in the equatorial thermocline are able to propagate to the surface, with values up to 0.5°C in the central Pacific Ocean. These values are comparable with those found by Farneti et al. (2014a) using an OGCM forced by the interannual CORE-II forcing during the period 1948–2007.

Subtropical wind stress anomalies produce the largest values of STC mass and energy transport anomalies. Overall, subtropical zonal wind stress anomalies are found to be the strongest forcing mechanism of STCs in the Pacific Ocean, as predicted by previous theoretical studies (e.g., McCreary and Lu 1994). On the other hand, extratropical wind stress anomalies are also capable of driving a substantial response in the overturning cells. Nevertheless, the signal reaching the

Equator is generated within the 15°-20° region, at the equatorward edge of the subtropical gyre, whereas any anomalous transport generated north of that latitude recirculated within the gyre.

The agreement between the regression lines and our key metrics in Fig. 15 supports a linear relationship with the applied wind stress forcing (angular coefficients are showed for each regression line). Subtropical experiments show a symmetric behavior between strengthened and weakened experiments, in both equatorward mass transport and STC energy transport. Instead, equatorial SST anomalies induced by the equatorial experiments does not show similar behaviors for strengthened and weakened experiments, making harder the interpretation of the STCs influence on SST in terms of a linear response.

Among the different processes connecting the Subtropics to the tropical ocean, our experiments suggest the interaction mechanism proposed by Kleeman et al. (1999) is able to explain remotely-driven thermal anomalies at the Equator in terms of anomalous STCs mass transports. That is, an anomalous STC transport drives a surface thermal signal at the Equator by altering the feeding of subsurface water to the thermocline. Our subtropical experiments drive a substantial STC response in the equatorial thermocline, where the bulk of the Equatorial Undercurrent flows and forms part of the returning branch of the STC circulation.

Indeed, ocean heat content anomalies in the equatorial Pacific Ocean (10°N-10°S), integrated at different depths during the final stage of the simulation for strengthened experiments (see Tab. 2), show a strong heat content increase in the first 300 m for the equatorial set, accounting for the whole increase in the total ocean column. Furthermore, the ITF advects part of the generated signal into the Indian Ocean, leading to significant heat content anomalies in the top 1000 m for all equatorial experiments (not shown). In the strengthened subtropical experiments, a negative heat content anomaly is generated, since a strengthened STC circulation draws deeper (and colder)

water to the surface, as shown in Fig. 8. Again, the heat content change is mostly located in the uppermost 300 meters.

The response given by the subtropical sector of the COWL pattern confirms what was obtained with our idealized experiments. Furthermore, it suggests a potential impact of mid-latitude atmospheric modes for STCs decadal variability. In fact, although fast processes play a leading role in forcing the STCs at short timescales, signals generated by low-frequency atmospheric variability, however small, are much more important at longer timescales.

Our experimental set-up proved very useful in highlighting some fundamental properties of STC dynamics and its connection to the tropical ocean. However, the time-independent wind stress anomalies applied and the absence of ocean-atmosphere coupling are strong limitations to our study. We plan to address these shortcomings in a follow-up study, investigating STCs variability in state-of-the-art coupled ocean-atmosphere models.

Acknowledgments. Thanks to the Center of Excellence for Climate Change Research (KAU University) for providing funds for this publication. The CORE datasets are collaboratively supported by the National Center for Atmospheric Research (NCAR) and the Geophysical Fluid Dynamics Laboratory (GFDL) under the umbrella of the Climate Variability and Predictability (CLIVAR) Working Group on Ocean Model Development (WGOMD). All datasets, codes for the bulk formulas, technical report, and other support codes along with the release notes are freely available at http://data1.gfdl.noaa.gov/nomads/forms/core.html.

APPENDIX A

Meridional energy transport by the SubTropical Cells

The momentum balance in the Ekman boundary layer is expressed as (Vallis 2006)

$$f\,\mathbf{k}\times\mathbf{u}_{\mathrm{E}}=\frac{1}{\rho_0}\frac{\partial\boldsymbol{\tau}}{\partial z}, \tag{A1}$$

where f is the Coriolis parameter, $\mathbf{u}_{\mathrm{E}}$ is the horizontal velocity vector in the Ekman layer, $\boldsymbol{\tau}$ the surface wind stress, ρ_0 a reference density and $\mathbf{k}$ the unit vertical direction.

Vertically integrating Eq. A1 yields

$$f\,\mathbf{k}\times\mathbf{M}_{\mathrm{E}}=\boldsymbol{\tau}, \tag{A2}$$

and the integrated mass transport in the Ekman layer is

$$\mathbf{M}_{\mathrm{E}}=\int_{h_e}^{0}\rho_0\mathbf{u}_{\mathrm{E}}\,\mathrm{d}z=\frac{\boldsymbol{\tau}\times\mathbf{k}}{f}, \tag{A3}$$

where h_e is the characteristic depth of the Ekman layer and Eq. A3 defines the Ekman transport to be proportional to the magnitude of the wind stress.

Suppose now the wind stress to be zonal $\tau(y)$, providing a meridional mass flux $\mathrm{M_E}=-\tau(y)/f(y)$. The wind stress τ is a function of latitude, generating a flow divergence at the surface and implying subduction into the ocean interior. Over a latitudinal interval δy, and using mass conservation, the mass flux subducted $\mathrm{M_S}$ is

$$\mathrm{M_S}=\frac{\partial \mathrm{M_E}}{\partial y}\delta y. \tag{A4}$$

If a latitude at which $\tau=0$ exists, as observed, then mass conservation requires all Ekman mass flux to be subducted. The flow beneath the Ekman layer exactly balances the mass flux in the Ekman layer, and the subducted mass flux $\mathrm{M_S}$ is equal and opposite to the Ekman mass flux $\mathrm{M_E}$. Considering a full latitudinal extent

$$\mathrm{M_S}=\int_{y}^{y_1}\frac{\partial \mathrm{M_E}}{\partial y}\,\mathrm{d}y=-\mathrm{M_E}(y), \tag{A5}$$

where y_1 is a subtropical subduction latitude at which $\tau = 0$ and we have noted that $\mathrm{M_E}(y_1) = 0$.

The temperature of the Ekman flow is $\theta(y)$, whereas the subducted flow conserves the surface temperature $\theta(y_1)$, assuming an interior adiabatic flow. The temperature flux associated with the Ekman flow is thus $\mathrm{T}_E(y) = \theta(y)\mathrm{M_E}$, whereas the returning branch of the circulation has a temperature flux given by

$$\mathrm{T}_S(y) = -\int_y^{y_1} \theta(y) \frac{\partial \mathrm{M_E}}{\partial y}\,\mathrm{d}y. \tag{A6}$$

The net temperature flux, which we relate to the STC, is given by Klinger and Marotzke (2000) and Held (2001) as

$$\begin{aligned} \mathrm{T_{STC}}(y) &= \theta(y)\mathrm{M_E} + \int_y^{y_1} \theta(y) \frac{\partial \mathrm{M_E}}{\partial y}\,\mathrm{d}y & \text{(A7)} \\ &= -\int_y^{y_1} \mathrm{M_E} \frac{\partial \theta}{\partial y}\,\mathrm{d}y = \int_y^{y_1} \frac{\tau(y)}{f} \frac{\partial \theta}{\partial y}\,\mathrm{d}y. & \text{(A8)} \end{aligned}$$

Or, in θ-space

$$\mathrm{T_{STC}}(y) = -\int_y^{y_1} \mathrm{M_E} \frac{\partial \theta}{\partial y}\,\mathrm{d}y = \int_{y_1}^{y} \mathrm{M_E} \frac{\partial \theta}{\partial y}\,\mathrm{d}y = \int_{\theta(y_1)}^{\theta(y)} \mathrm{M_E}\,\mathrm{d}\theta. \tag{A9}$$

The last expression is the same as Eq. 11 in Klinger and Marotzke (2000) and Eq. 8 in Held (2001).

The meridional energy transport of the subtropical cell is obtained by zonally integrating the temperature flux and multiplying by C_p, the heat capacity of the ocean

$$\mathrm{E_{STC}}(y) = C_\mathrm{p} \int_{\lambda_1}^{\lambda_2} \mathrm{d}x \int_{y_1}^{y} \mathrm{M_E} \frac{\partial \theta}{\partial y}\,\mathrm{d}y. \tag{A10}$$

References

Broccoli, A., N. Lau, and M. Nath, 1998: The Cold Ocean - Warm Land pattern: Model simulation and relevance to climate change detection. *J. Climate*, **11**, 2743–2763, doi:10.1175/1520-0442(1998)011⟨2743:TCOWLP⟩2.0.CO;2.

Bryan, K., 1991: Poleward heat transport in the ocean: A review of a hierarchy of models of increasing resolution. *Tellus*, **43 (4)**, 104–115, doi:10.3402/tellusa.v43i4.11940.

Capotondi, A., M. Alexander, C. Deser, and M. McPhaden, 2005: Anatomy and decadal evolution of the Pacific Subtropical-Tropical Cells (STCs). *J. Climate*, **18 (18)**, 3739–3758.

Deser, C., M. Alexander, and M. Timlin, 1996: Upper-ocean thermal variations in the North Pacific during 1970-1991. *J. Climate*, **9 (8)**, 1840–1855.

England, M., and F. Huang, 2005: On the interannual variability of the Indonesian Throughflow and its linkage with ENSO. *J. Climate*, **18 (9)**, 1435–1444.

England, M., S. McGregor, P. Spence, G. Meehl, A. Timmermann, . W. Cai, and A. Santoso, 2014: Recent intensification of wind-driven circulation in the Pacific and the ongoing warming hiatus. *Nature Clim. Change*, **4 (3)**, 222–227.

Farneti, R., S. Dwivedi, F. Kucharski, F. Molteni, and G. Griffies, 2014a: On Pacific Subtropical Cell variability over the second half of the twentieth century. *J. Climate*, **27**, 7102–7112, doi:10.1175/JCLI-D-13-00707.1.

Farneti, R., F. Molteni, and F. Kucharski, 2014b: Pacific interdecadal variability driven by tropical-extratropical interactions. *Clim. Dyn.*, **42 (11-12)**, 3337–3355.

Fox-Kemper, B., R. Ferrari, and R. Hallberg, 2008: Parameterization of mixed layer eddies. Part I: Theory and diagnosis. *J. Phys. Oceanogr.*, **38**, 1145–1165, doi:10.1175/2007JPO3792.1.

Fox-Kemper, B., and Coauthors, 2011: Parameterization of mixed layer eddies. Part III: Implementation and impact in global ocean climate simulations. *Ocean Modelling*, **39**, 61–78, URL https://doi.org/10.1016/j.ocemod.2010.09.002.

Gent, P., and J. Mcwilliams, 1990: Isopycnal mixing in ocean circulation models. *J. Phys. Oceanogr.*, **20**, 150–155, doi:10.1175/1520-0485(1990)020⟨0150:IMIOCM⟩2.0.CO;2.

Gent, P., J. Willebrand, T. McDougall, and J. McWilliams, 1995: Parameterizing eddy-induced tracer transports in ocean circulation models. *J. Phys. Oceanogr.*, **25**, 463–474, doi:10.1175/1520-0485(1995)025⟨0463:PEITTI⟩2.0.CO;2.

Griffies, S., 1998: The Gent-McWilliams skew flux. *J. Phys. Oceanogr.*, **28**, 831–841, doi:10.1175/1520-0485(1998)028⟨0831:TGMSF⟩2.0.CO;2.

Griffies, S., 2012: *Elements of the Modular Ocean Model (MOM)*. Princeton (NJ), USA, NOAA Geophysical Fluid Dynamics Laboratory.

Griffies, S., A. Biastoch, C. Böning, F. Bryan, G. Danabasoglu, E. Chassignet, ..., and W. Hazeleger, 2009: Coordinated Ocean-ice Reference Experiments (COREs). *Ocean Modelling*, **26 (1)**, 1–46.

Gu, D., and S. Philander, 1997: Interdecadal climate fluctuations that depend on exchanges between the tropics and extratropics. *Science*, **275 (5301)**, 805–807.

Hazeleger, W., P. de Vries, and G. van Oldenborgh, 2000: Do Tropical Cells ventilate the Indo-Pacific equatorial thermocline? *Geophys. Res. Lett.*, **28 (9)**, 1763–1766.

Held, I., 2001: The partitioning of the poleward energy transport between the tropical ocean and atmosphere. *J. Atmos. Sci.*, **58**, 943–948, doi:10.1175/1520-0469(2001)058⟨0943:TPOTPE⟩2.0.CO;2.

586 Hong, L., L. Zhang, Z. Chen, and L. Wu, 2014: Linkage between the Pacific Decadal Oscillation
587 and the low frequency variability of the Pacific Subtropical Cell. *J. Geophys. Res.: Oceans*, **119**,
588 3464–3477, doi:10.1002/2013JC009650.

589 Jayne, S., and J. Marotzke, 2001: The dynamics of ocean heat transport variability. *Rev. Geophys.*,
590 **39 (3)**, 385–411, doi:10.1029/2000RG000084.

591 Johnson, G., 2001: The Pacific Ocean Subtropical Cell surface limb. *Geophys. Res. Lett.*, **28 (9)**,
592 1771–1774, doi:10.1029/2000GL012723.

593 Johnson, G., and M. McPhaden, 1999: Interior pycnocline flow from the subtropical to the equa-
594 torial Pacific Ocean. *J. Phys. Oceanogr.*, **29 (12)**, 3073–3089.

595 Kleeman, R., J. McCreary, and B. Klinger, 1999: A mechanism for generating ENSO decadal
596 variability. *Geophys. Res. Lett.*, **26 (12)**, 1743–1746.

597 Klinger, B., and J. Marotzke, 2000: Meridional heat transport by the Subtropical Cell. *J. Phys.*
598 *Oceanogr.*, **30 (4)**, 696–705.

599 Klinger, B., J. McCreary, and R. Kleeman, 2002: The relationship between oscillating sub-
600 tropical wind stress and equatorial temperature. *J. Phys. Oceanogr.*, **32**, 1507–1521, doi:
601 10.1175/1520-0485(2002)032⟨1507:TRBOSW⟩2.0.CO;2.

602 Large, W., and S. Yeager, 2009: The global climatology of an interannually varying air-sea flux
603 data set. *Clim. Dyn.*, **33 (2)**, 341–364, doi:10.1007/s00382-008-0441-3.

604 Lee, T., and I. Fukumori, 2003: Interannual-to-decadal variations of tropical-subtropical exchange
605 in the Pacific Ocean: Boundary versus interior pycnocline transports. *J. Climate*, **16**, 4022–
606 4042, doi:10.1175/1520-0442(2003)016⟨4022:IVOTEI⟩2.0.CO;2.

607 Liu, Z., 1994: A simple model of the mass exchange between the subtropical and tropical ocean.
608 *J. Phys. Oceanogr.*, **24 (6)**, 1153–1165.

609 Liu, Z., and M. Alexander, 2007: Atmospheric bridge, oceanic tunnel and global climatic telecon-
610 nections. *Rev. Geophys.*, **45**, RG2005, doi:10.1029/2005RG000172.

611 Liu, Z., and S. Philander, 1995: How different wind stress patterns affect the tropical-subtropical
612 circulations of the upper ocean. *J. Phys. Oceanogr.*, **25**, 449–462, doi:10.1175/1520-0485(1995)
613 025⟨0449:HDWSPA⟩2.0.CO;2.

614 Liu, Z., S. Philander, and R. Pacanowski, 1994: A GCM study of tropical–subtropical upper-ocean
615 water exchange. *J. Phys. Oceanogr.*, **24**, 2606–2623, doi:10.1175/1520-0485(1994)024⟨2606:
616 AGSOTU⟩2.0.CO;2.

617 Lu, P., and J. McCreary, 1995: Influence of the ITCZ on the flow of thermocline water from the
618 subtropical to the equatorial Pacific Ocean. *J. Phys. Oceanogr.*, **25**, 3076–3088, doi:10.1175/
619 1520-0485(1995)025⟨3076:IOTIOT⟩2.0.CO;2.

620 Lu, P., J. McCreary, and B. Klinger, 1998: Meridional circulation cells and the source waters of
621 the Pacific Equatorial Undercurrent. *J. Phys. Oceanogr.*, **28 (1)**, 62–84.

622 McCreary, J., and P. Lu, 1994: Interaction between the subtropical and equatorial ocean circula-
623 tions: The Subtropical Cell. *J. Phys. Oceanogr.*, **24 (2)**, 466–497.

624 McGregor, S., N. Holbrook, and S. Power, 2007: Interdecadal sea surface temperature variability
625 in the equatorial pacific ocean. Part I: The role of off-equatorial wind stresses and oceanic rossby
626 waves. *J. Climate*, **20**, 2643–2658, doi:10.1175/JCLI4145.1.

627 McPhaden, M., and D. Zhang, 2002: Slowdown of the meridional overturning circulation in the
628 upper Pacific Ocean. *Nature*, **415 (6872)**, 603–608.

McPhaden, M., and D. Zhang, 2004: Pacific Ocean circulation rebounds. *Geophys. Res. Lett.*, **31**, doi:10.1029/2004GL020727.

Meehl, G., A. H. J. Arblaster, J. Fasullo, and K. Trenberth, 2013: Externally forced and internally generated decadal climate variability associated with the Interdecadal Pacific Oscillation. *J. Climate*, **26 (18)**, 7298–7310, doi:10.1175/JCLI-D-12-00548.1.

Meyers, G., 1996: Variation of Indonesian Throughflow and the El Niño Southern Oscillation. *J. Geophys. Res.: Oceans*, **101 (C5)**, 12 255–12 263.

Molinari, R., S. Bauer, D. Snowden, G. J. B. Bourles, Y. Gouriou, and H. Mercier, 2003: A comparison of kinematic evidence for Tropical Cells in the Atlantic and Pacific Oceans. *Elsevier Ocean. Ser.*, **68**, 269–286.

Molteni, F., R. Farneti, F. Kucharski, and T. Stockdale, 2017: Modulation of air-sea fluxes by extratropical planetary waves and its impact during the recent surface warming slowdown. *Geophys. Res. Lett.*, **44**, 1494–1502, doi:10.1002/2016GL072298.

Molteni, F., M. King, F. Kucharski, and D. Straus, 2011: Planetary-scale variability in the northern winter and the impact of land-sea thermal contrast. *Clim. Dyn.*, **37 (1)**, 151–170, doi:10.1007/s00382-010-0906-z.

Nakano, H., R. Furue, and N. Suginohara, 1999: Effect of seasonal forcing on global circulation in a World Ocean general circulation model. *Clim. Dyn.*, **15 (7)**, 491–502, doi:10.1007/s003820050295.

Nonaka, M., S. Xie, and J. McCreary, 2002: Decadal variations in the Subtropical Cells and equatorial Pacific SST. *Geophys. Res. Lett.*, **29 (7)**, 201–204, doi:10.1029/2001GL013717.

650 Pedlosky, J., 1987: An inertial theory of the Equatorial Undercurrent. *J. Phys. Oceanogr.*, **17**,
651 1978–1985, doi:10.1175/1520-0485(1987)017⟨1978:AITOTE⟩2.0.CO;2.

652 Power, S., T. Casey, C. Folland, A. Colman, and V. Mehta, 1999: Inter-decadal modulation of the
653 impact of ENSO on Australia. *Clim. Dyn.*, **15 (5)**, 319–324, doi:10.1007/s003820050284.

654 Schneider, N., A. M. M. Alexander, and C. Deser, 1999: Subduction of decadal North Pacific
655 temperature anomalies: Observations and dynamics. *J. Phys. Oceanogr.*, **29 (5)**, 1056–1070.

656 Schott, F., J. McCreary, and G. Johnson, 2004: Shallow overturning circulations of the tropical-
657 subtropical oceans. *Earth's Climate*, S. X. C. Wang, and J. Carton, Eds., American Geophysical
658 Union, Washington D.C., USA, doi:10.1029/147GM15.

659 Schott, F., L. Stramma, W. Wang, B. Giese, and R. Zantopp, 2008: Pacific Subtropical Cell
660 variability in the SODA 2.0.2/3 assimilation. *Geophys. Res. Lett.*, **35**, L10 607, doi:10.1029/
661 2008GL033757.

662 Schott, F., W. Wang, and D. Stammer, 2007: Variability of Pacific Subtropical Cells in the 50-year
663 ECCO assimilation. *Geophys. Res. Lett.*, **34**, L05 604, doi:10.1029/2006GL028478.

664 Solomon, A., J. McCreary, R. Kleeman, and B. Klinger, 2003: Interannual and decadal variability
665 in an intermediate coupled model of the Pacific region. *J. Climate*, **16**, 383–405, doi:10.1175/
666 1520-0442(2003)016⟨0383:IADVIA⟩2.0.CO;2.

667 Solomon, A., and D. Zhang, 2006: Pacific subtropical cell variability in coupled climate model
668 simulations of the late 19th-20th century. *Ocean Modelling*, **15**, 236–249, doi:10.1016/j.
669 ocemod.2006.03.007.

670 Vallis, G., 2006: *Atmospheric and oceanic fluid dynamics*. Cambridge Univ. Press.

671 Wallace, J., Y. Zhang, and L. Bajuk, 1996: Interpretation of interdecadal trends in Northern Hemi-
672 sphere surface air temperature. *J. Climate*, **9**, 249–259, doi:10.1175/1520-0442(1996)009⟨0249:
673 IOITIN⟩2.0.CO;2.

674 Wallace, J., Y. Zhang, and J. Renwick, 1995: Dynamic contribution to hemispheric mean temper-
675 ature trends. *Science*, **270 (5237)**, 780–783, doi:10.1126/science.270.5237.780.

676 Wyrtki, K., and B. Kilonsky, 1984: Mean water and current structure during the Hawaii-to-Tahiti
677 Shuttle Experiment. *J. Phys. Oceanogr.*, **14**, 242–254, doi:10.1175/1520-0485(1984)014⟨0242:
678 MWACSD⟩2.0.CO;2.

679 Zhang, D., and M. McPhaden, 2006: Decadal variability of the shallow Pacific meridional over-
680 turning circulation: Relation to tropical sea surface temperatures in observations and climate
681 change models. *Ocean Modelling*, **15 (3)**, 250–273, doi:10.1016/j.ocemod.2005.12.005.

682 Zhang, Y., J. Wallace, and D. Battisti, 1997: ENSO-like interdecadal variability: 1900-93. *J.*
683 *Climate*, **10 (5)**, 1004–1020.

LIST OF TABLES

TABLE 1. Main characteristics of the idealized perturbation experiments. τ_x is the zonal wind stress applied to the ocean surface during each experiment. The ocean model computes the zonal wind stress from the climatological zonal wind (NYF). Then, during the perturbation experiments, an anomaly is added to the climatological wind stress as a fraction, positive or negative, of the wind stress itself.

Experiment	τ_x	Time (years)
Control	NYF	1400
10	NYF$\pm$10%	20
20	NYF$\pm$20%	20
30	NYF$\pm$30%	20
40	NYF$\pm$40%	20
50	NYF$\pm$50%	20

700 TABLE 2. Ocean heat content anomaly (10^{21} J) in the equatorial Pacific Ocean (10°N-10°S) resulting from
701 equatorial and north subtropical strengthened experiments. Values are given for the upper 300 m, upper 1000 m
702 and the total water column. Only the weakest and strongest wind stress anomaly experiments are considered.

	Equatorial		Subtropical	
Depth	10%	50%	10%	50%
0 - 300 m	154	717	-52.5	-275
0 - 1000 m	153	717	-56	-284
Total	153	717	-55.5	-280

LIST OF FIGURES

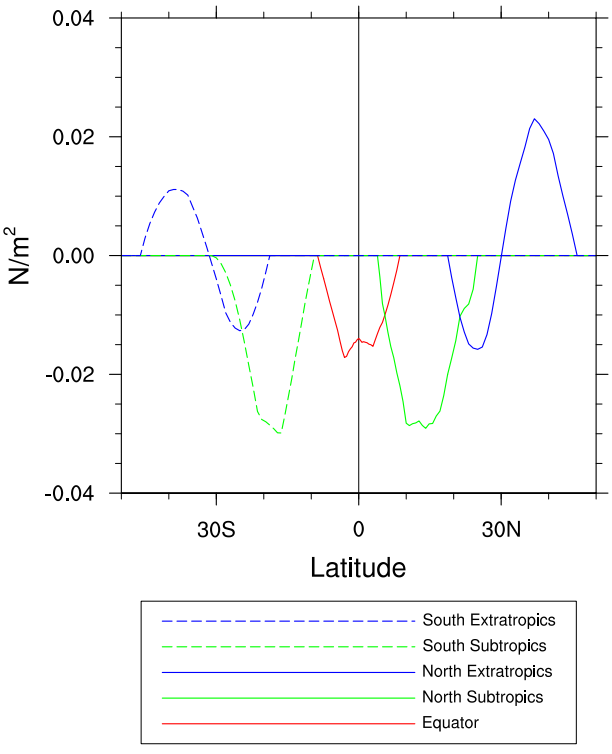

FIG. 1. Zonal average of the zonal wind stress anomalies (N/m^2), computed from the climatological value of the zonal wind stress from the CORE-I dataset (Griffies et al. 2009). Each anomaly is added or subtracted to the NYF, after been multiplied by a factor.

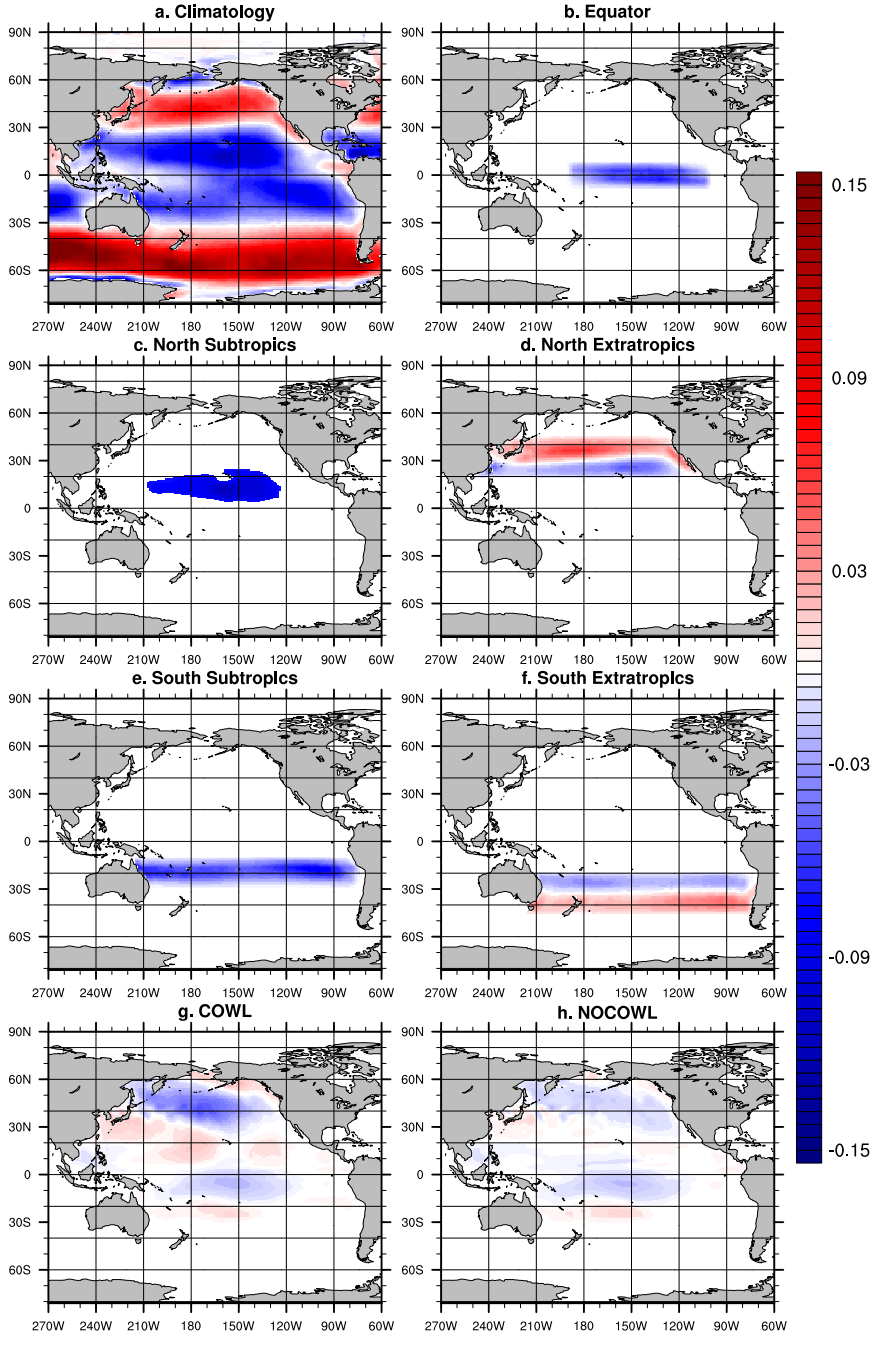

FIG. 2. Climatological zonal wind stress (N/m^2), zonal wind stress anomalies and their location. Panels a-f: climatological values of the zonal wind stress from the CORE-I dataset (Griffies et al. 2009), which are multiplied by a factor and then added to or subtracted from the applied wind stress field. Panels g-h: ensemble means obtained from the ECMWF seasonal forecast System-4 (Molteni et al. 2011). One ensemble-mean is representative of observed decadal changes that can be described by a shift of the COWL-like pattern (Molteni et al. 2017), and is composed of members reproducing closely the observed COWL anomalies (*COWL*; panel g). The second ensemble-mean stems from members whose response along the COWL pattern is close to zero (*NOCOWL*; panel h).

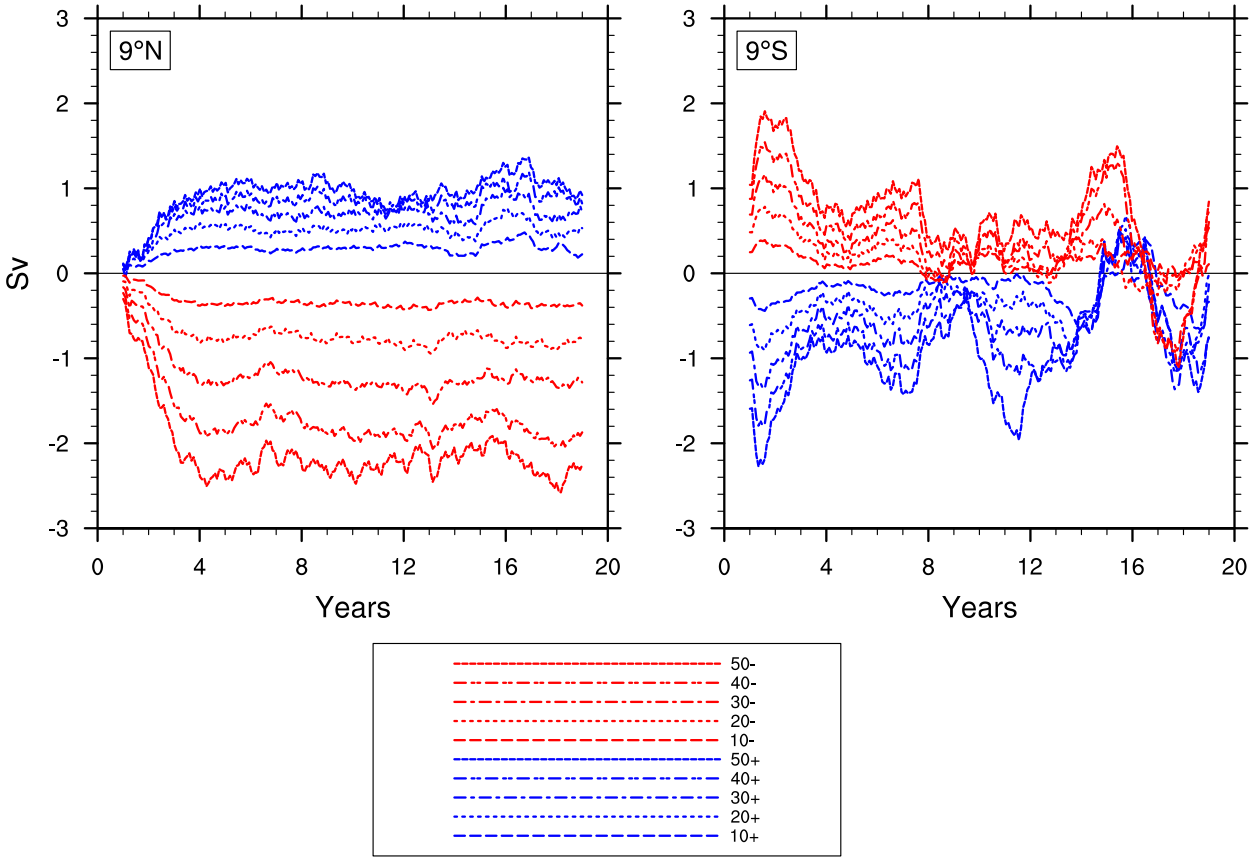

780 FIG. 3. Time series (25-months running mean) of the zonally and vertically-integrated anomalous equatorward
781 transport (Sv) for the equatorial experiments at 9° of each hemisphere in the Indo-Pacific Ocean. Anomalies are
782 computed as deviations from the control value. In the legend, + refers to strengthened anomalies and - to
783 weakened anomalies.

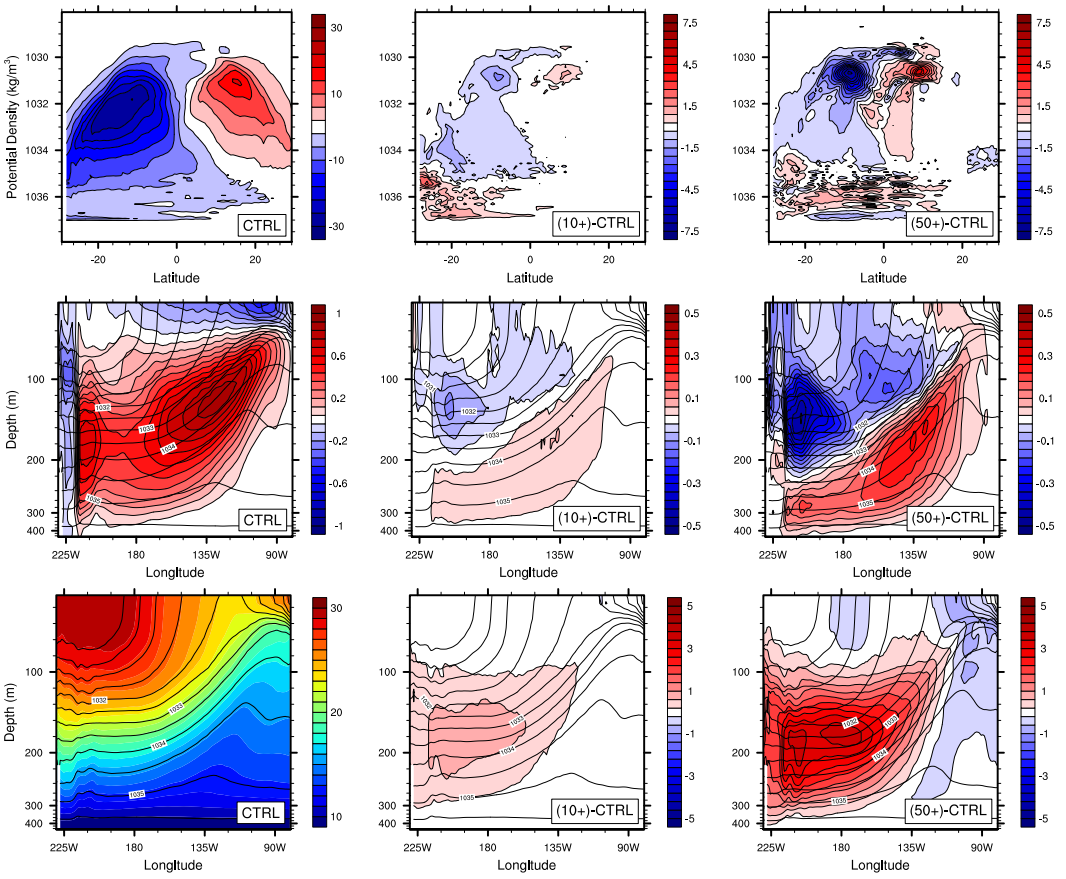

FIG. 4. (Top panels) Zonally-integrated mass transport on potential density coordinates (kg m^{-3}, referred to 2000 dbar) over the Indo-Pacific Ocean. Time-mean overturning (left), 10% (center) and 50% (right) anomalies for the strengthened equatorial experiments. Red structures are clock-wise cells and blue ones are counterclock-wise. Units are Sverdrup (1 Sv = 10^6 m^3 s^{-1}). (Central panels) Zonal cross sections of zonal velocity (m/s) at the Equator for the control run (left panels, contours), and anomalies for the 10% and 50% (middle and right panels, contours) strengthened equatorial experiments, superimposed on isolines of potential density (kg m^{-3}, referred to 2000 dbar). (Bottom panels) Zonal cross sections of temperature (°C) at the Equator for the control run (left panels, contours), and anomalies for the 10% and 50% (middle and right panels, contours) strengthened equatorial experiments, superimposed on isolines of potential density (kg m^{-3}, referred to 2000 dbar).

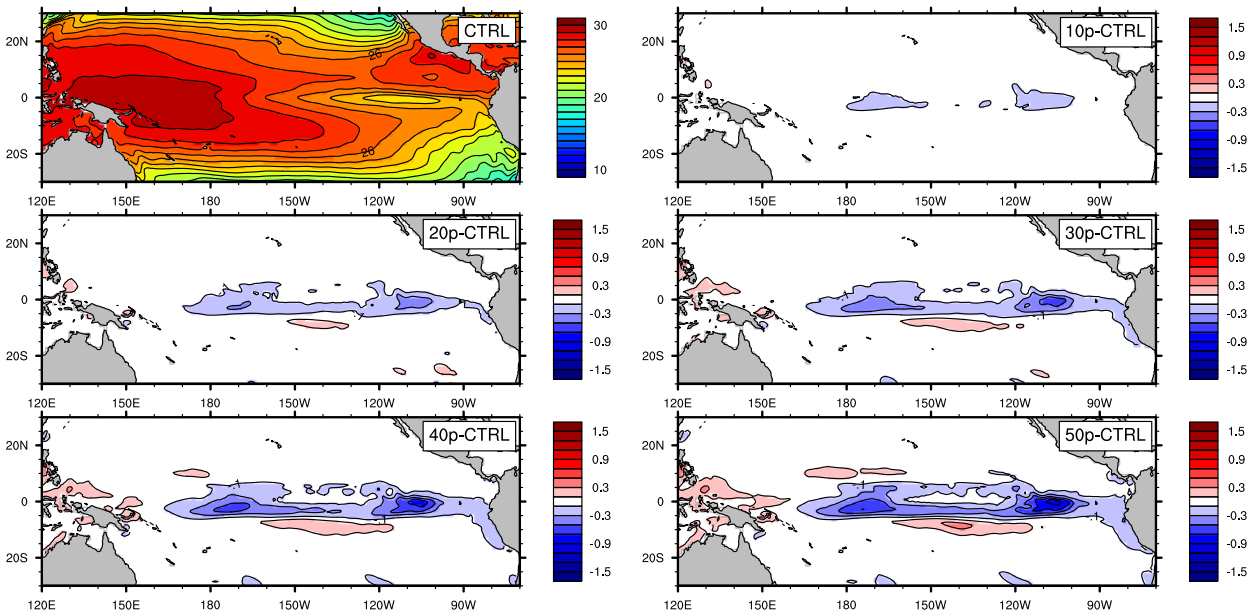

793 FIG. 5. Sea surface temperature (°C) for the control run (top-left panel), and anomalies for the strengthened
794 equatorial experiments.

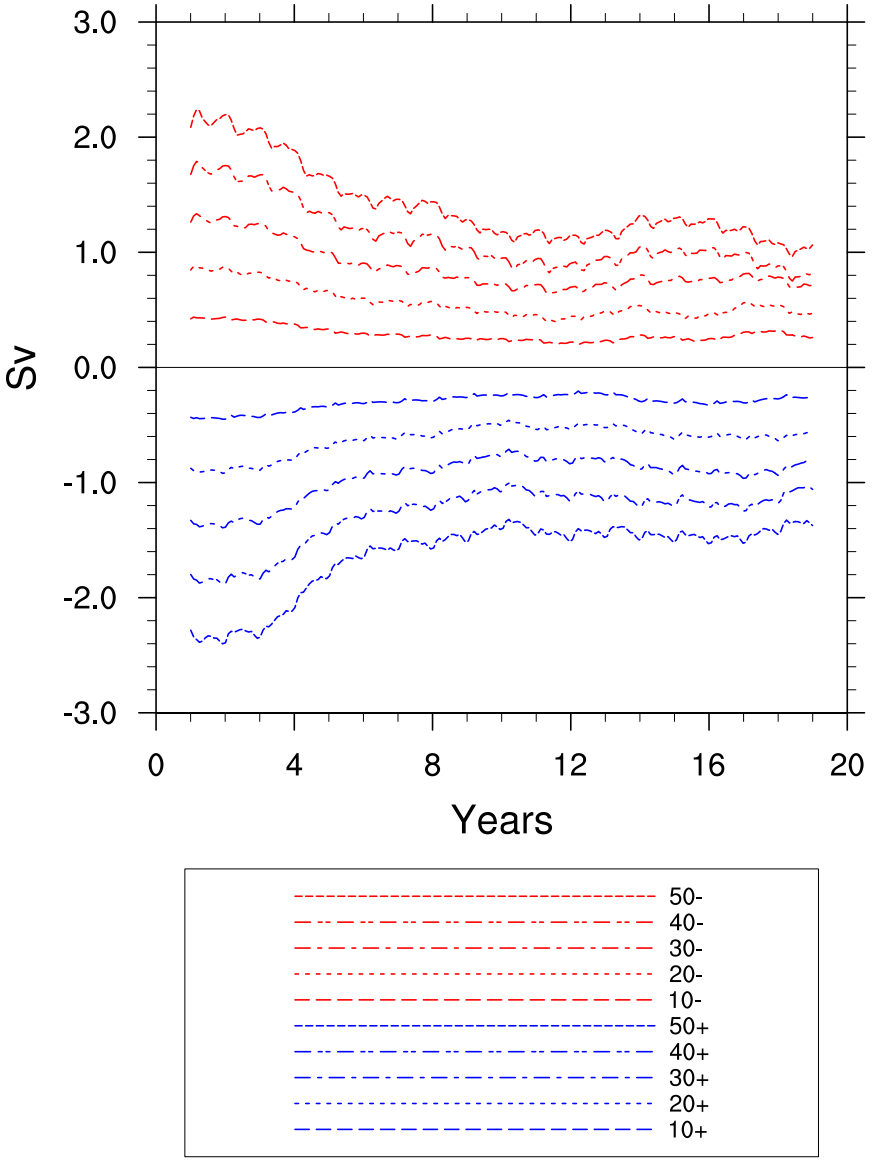

795 FIG. 6. Time series (25-months running mean) of the Indonesian ThroughFlow mass transport (Sv) for the
796 equatorial experiments, shown as anomalies relative to the control run. In the legend, + refers to strengthened
797 anomalies and - to weakened anomalies.

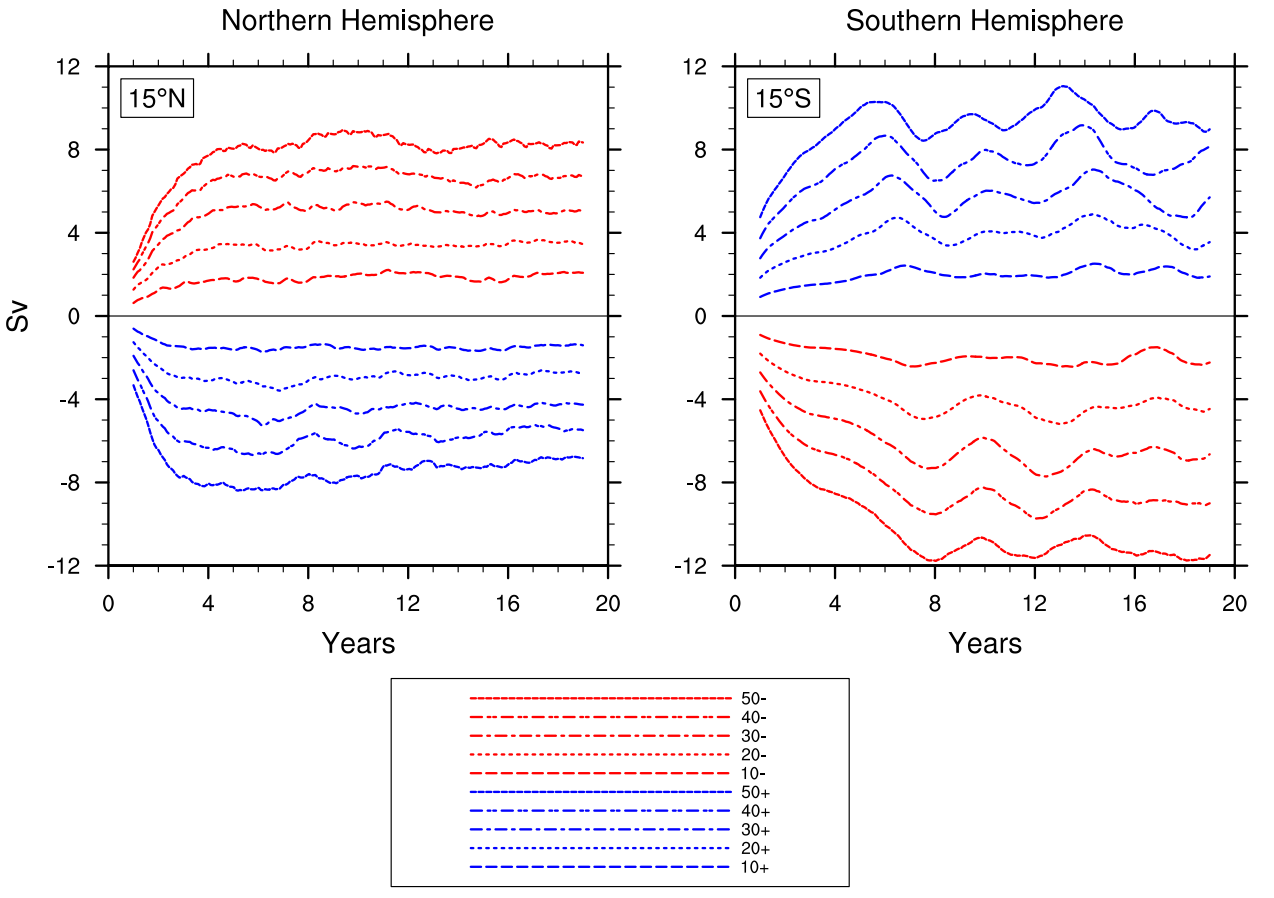

798 FIG. 7. As in Fig. 3 but for the northern subtropical (left panel) and the southern subtropical (right panel)
799 experiments at 15° of each hemisphere in the Indo-Pacific Ocean.

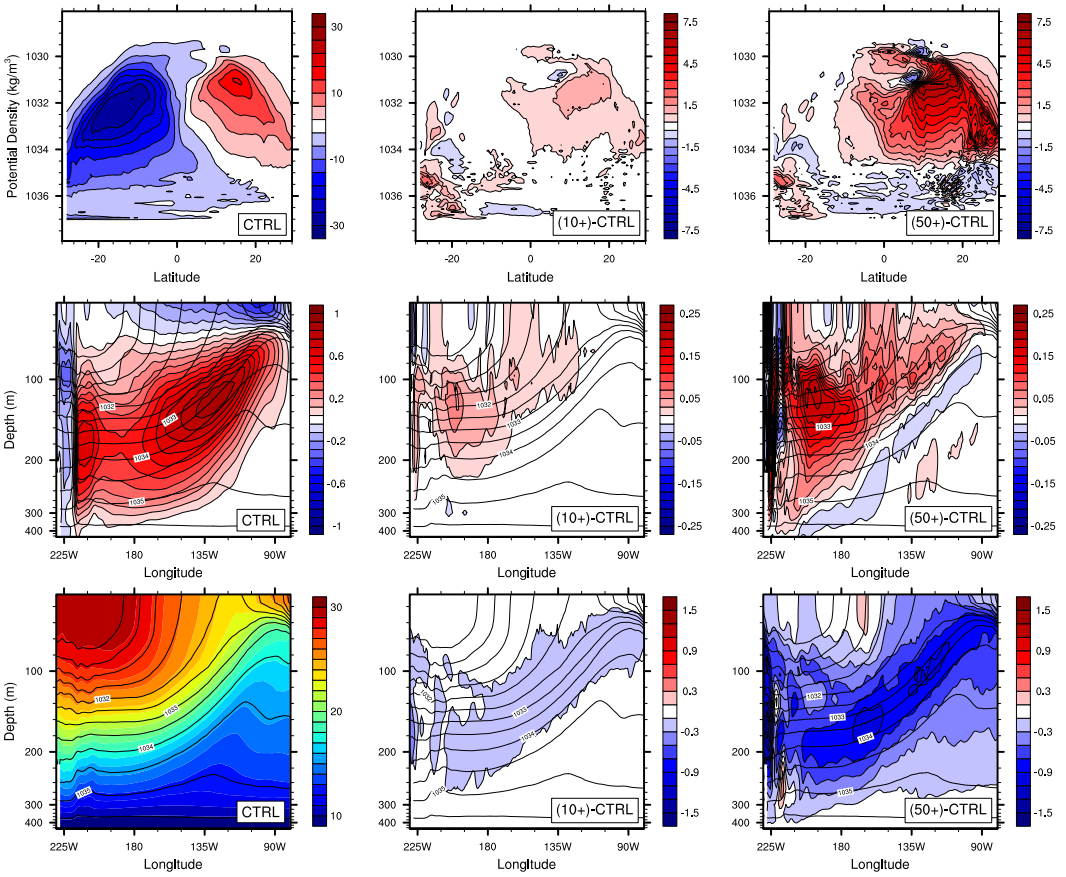

FIG. 8. As in Fig. 4 but for the northern subtropical experiments.

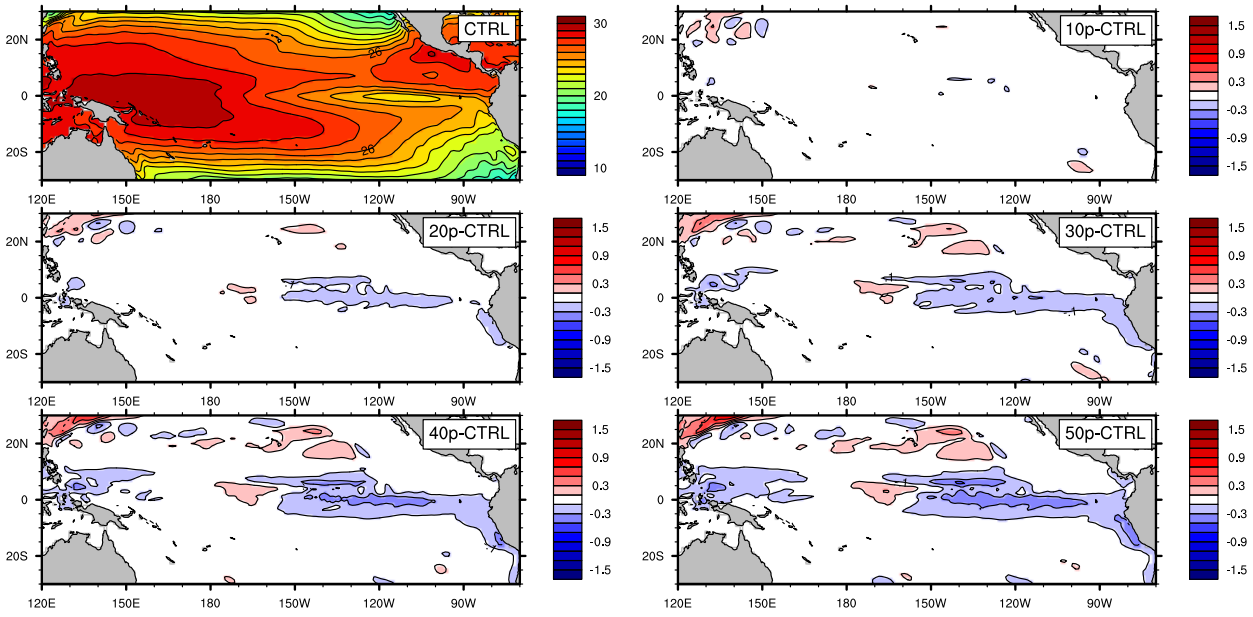

FIG. 9. As in Fig. 5 but for the northern subtropical experiments.

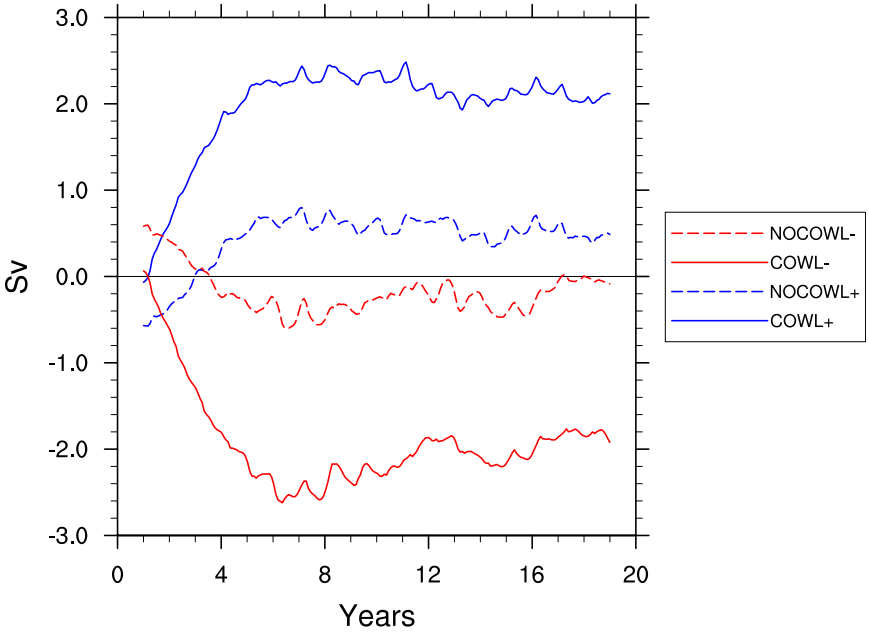

800 FIG. 10. Time series (25-months running mean) of the zonally and vertically-integrated anomalous equator-
801 ward transport (Sv) for the COWL experiments at 15° of each hemisphere in the Indo-Pacific Ocean. Anomalies
802 are computed as deviations from the control value. In the legend, *COWL+* and *COWL-* refer to strengthened and
803 weakened anomalies, respectively. *NOCOWL+* and *NOCOWL-* refer to the ensemble mean not projecting on the
804 COWL pattern (see text for more details).

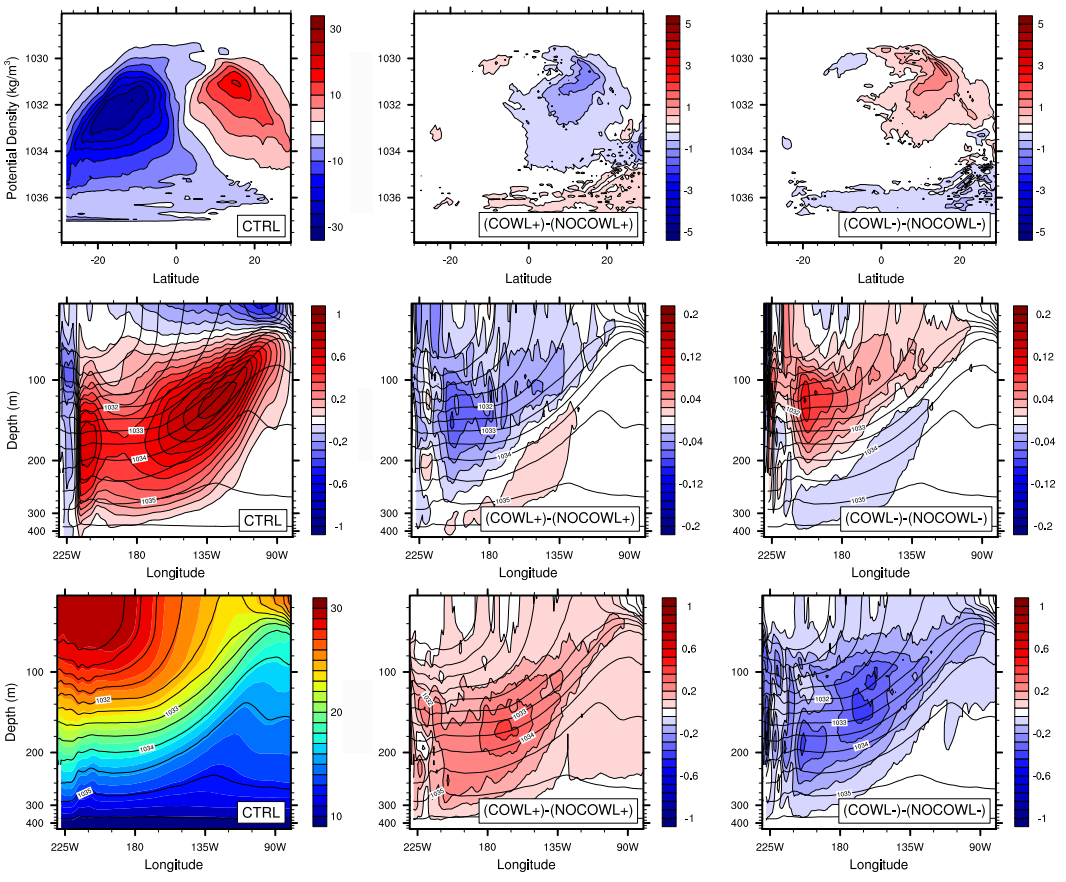

805 FIG. 11. As in Fig. 4 but for the realistic wind stress anomalies. Results are presented as the difference
806 between the ensemble-mean reproducing the COWL pattern (*COWL* experiment) minus the ensemble-mean not
807 projecting on COWL (*NOCOWL* experiment).

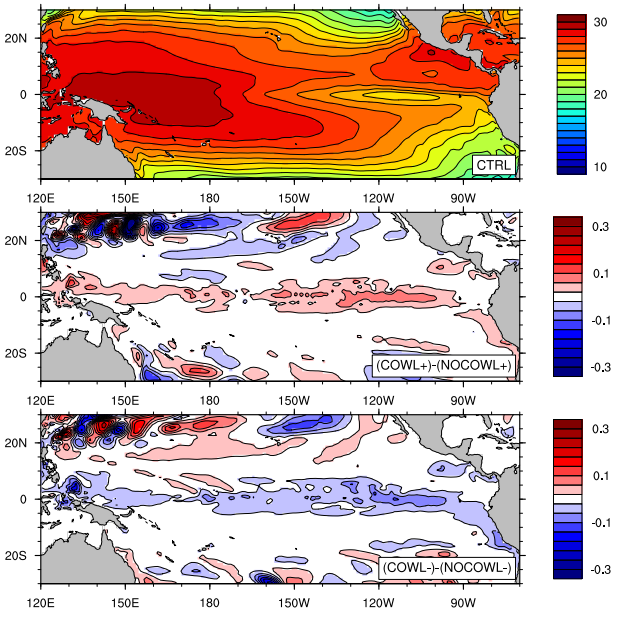

808 FIG. 12. As in Fig. 5 but for the realistic wind stress anomalies. Results are presented as the difference
809 between the ensemble-mean reproducing the COWL pattern (*COWL* experiment) minus the ensemble-mean not
810 projecting on COWL (*NOCOWL* experiment).

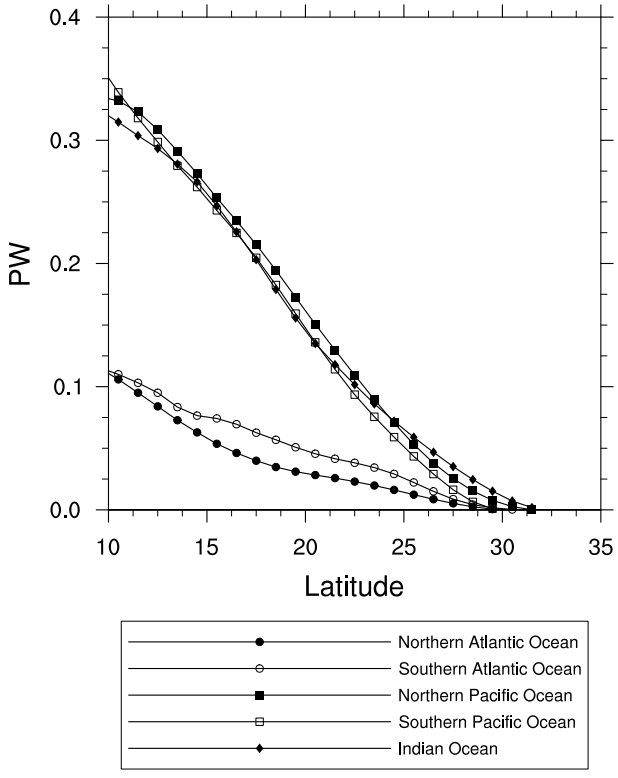

FIG. 13. STC meridional energy transports in the control run computed for all basins (1 PW = 10^{15} W). Transports are estimated using Eq. 4 and are in agreement with previous observational estimates (Klinger and Marotzke 2000, c.f. Fig. 6).

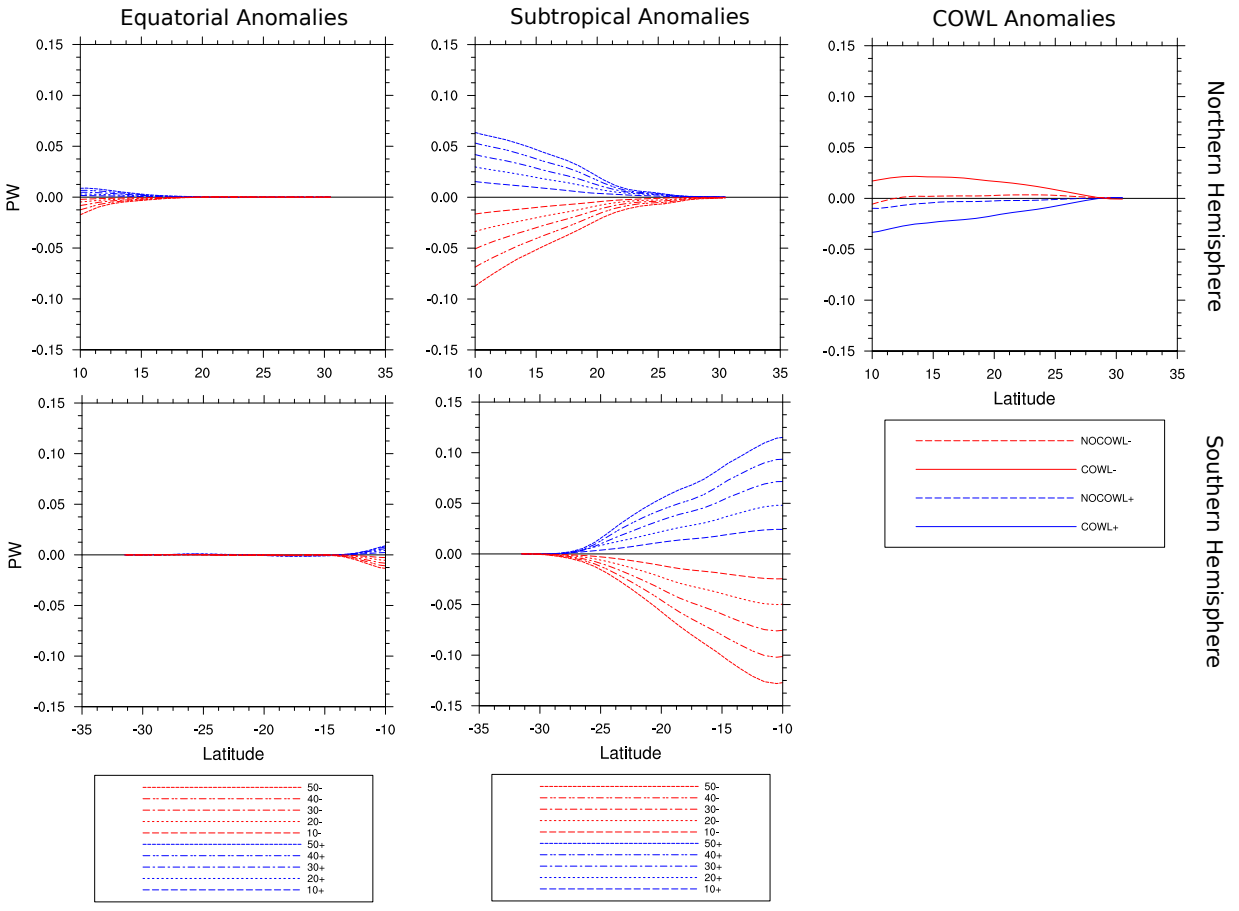

814 FIG. 14. STC meridional energy transport (1 PW = 10^{15} W) for all northern (top row) and southern (bottom
815 row) experiments, estimated using Eq. 4. Anomalies shown are for the equatorial (left column), subtropical
816 (middle column), and *COWL* (right column) experiments. In the legend, + refers to strengthened anomalies and
817 - to weakened anomalies.

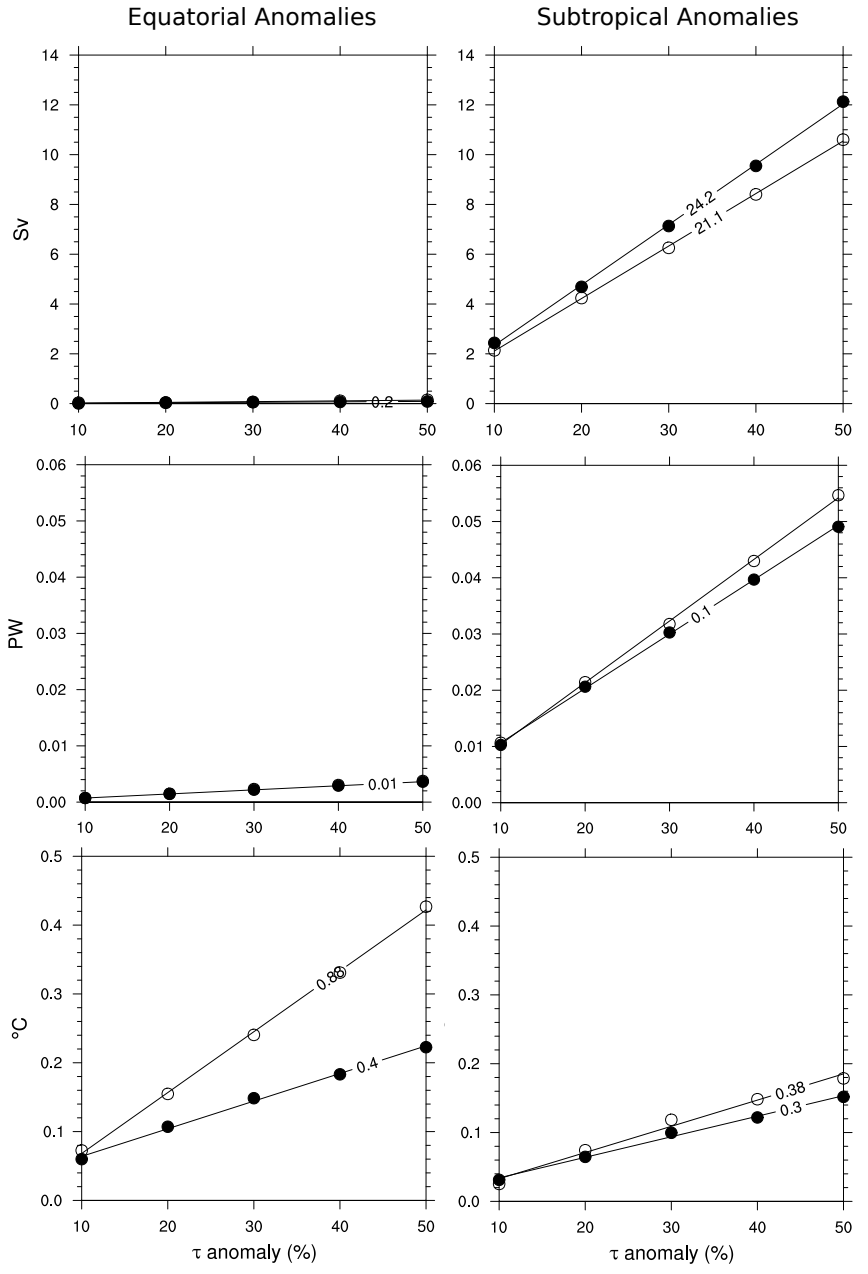

FIG. 15. Absolute value of anomalies in equatorward mass transport (top row), STC meridional energy transport (middle row) and equatorial SST (bottom row) plotted against wind stress anomaly for equatorial (left column) and subtropical (right column) wind stress patterns. Mass transports are evaluated as the maximum time-averaged, zonally-integrated, vertically-integrated equatorward mass transport anomaly in the region 10°-30°N. STC energy transport are evaluated as the time-averaged, zonally-integrated energy tranport anomaly at 15°N. Equatorial SST anomalies are evaluated in the Niño 3.4 region (5°N - 5°S, 120°- 170°W). Solid and empty circles denote strengthened and weakened experiments, respectively. Linear fits are showed for each experimental set, together with the angular coefficient a of the regression line $y = ax$.